



# Graphene monovacancies: Electronic and mechanical properties from large scale ab initio simulations



Lucía Rodrigo<sup>a</sup>, Pablo Pou<sup>a, b, \*</sup>, Rubén Pérez<sup>a, b</sup>

<sup>a</sup> Departamento de Física Teórica de la Materia Condensada, Universidad Autónoma de Madrid, ES-28049 Madrid, Spain

<sup>b</sup> Condensed Matter Physics Center (IFIMAC), Universidad Autónoma de Madrid, ES-28049 Madrid, Spain

## ARTICLE INFO

### Article history:

Received 14 October 2015

Received in revised form

11 January 2016

Accepted 22 February 2016

Available online 23 February 2016

## ABSTRACT

In this work we have carried out a complete set of large scale density functional theory simulations to characterize the magnetic and mechanical properties of graphene as a function of the monovacancy concentration. Our simulations on systems with up to a  $G(30 \times 30)$  cell size where we used several thousand k-point meshes –which make them a challenging computational problem– show a clear tendency to converge the local magnetic moment of monovacancies to  $2 \mu_B$  in the diluted limit. Our results confirm that the vacancies experience a Jahn-Teller distortion leading to a 5–9 asymmetric reconstruction and we find a transition to a more symmetric structure when an external isotropic in-plane strain beyond the 2% is applied. Regarding the mechanical properties, we conclude that, even when the presence of monovacancies does not practically affect the in-plane deformations, they induce a strain field that clearly quenches the out-of-plane vibrations, making the defective sample stiffer than its pristine version for a low concentration of vacancies. The 5–9 structure, responsible of this strain field, has been checked to be also stable at room temperature.

© 2016 Elsevier Ltd. All rights reserved.

## 1. Introduction

Graphene is a promising material due to its outstanding electronic and mechanical properties [1]. Real materials have defects which, instead of being a drawback, can be regarded as an opportunity to tune their properties. Defect engineering in graphene is nowadays an active and crucial research area [2–8]. Of particular interest is the influence of defects on both the mechanical properties and the tuning of electronic and magnetic properties of this material. Spintronics represents one of the most exciting fields for possible applications of graphene [2]. Monovacancies ( $V_1$ ), one of the most common defects on graphene [4], have been proposed to induce local magnetic moments in this carbon-based material [9–11]. Furthermore, recent measurements show that the mechanical properties are modified in an unexpected way: instead of contributing to a softness of the material, low concentrations of vacancies increase the graphene stiffness [12].

The removal of an atom from the graphene lattice leaves three equivalent C atoms with unsaturated  $\sigma$  bonds and the structure of

the  $V_1$  could remain in a symmetric arrangement ( $s-V_1$ ). However, density functional theory (DFT) simulations [4,9–11] predict a Jahn-Teller distortion by the formation of a soft  $\sigma$  bond between two of the C atoms which leads the  $V_1$  to an asymmetric 5–9 reconstruction ( $a-V_1$ ) with a formation energy in the range of 7.3–8.58 eV [4]. On the other hand, classical force fields [4,13] yield to a symmetric structure and no soft bond is formed due to the electronic nature of this reconstruction, which this computational scheme cannot account for.

The  $V_1$  have been observed by transmission electron microscope (TEM) studies [6,7,14–16]. Both  $a-V_1$  and  $s-V_1$  vacancy structures have been reported [16]. Scanning tunneling microscope (STM) experiments have also measured  $V_1$  on graphite and graphene on metals [17–19] where the atomic structure is distorted by the electronic effects but comparison with DFT simulations [18] support the presence of the  $a-V_1$  reconstruction.

According to previous works (see Ref. [2] and references therein), there are experimental evidences of magnetism in defected graphene sheets. Supporting these experimental results, DFT calculations on clusters or small cells (high  $V_1$  concentration) [4,9–11] predict the  $V_1$  to be magnetic. The explanation for this phenomena is straightforward in terms of the electron redistribution. Among the 3  $\sigma$  electrons that are now unpaired, 2 form a soft

\* Corresponding author. Departamento de Física Teórica de la Materia Condensada, Universidad Autónoma de Madrid, ES-28049 Madrid, Spain.

E-mail address: [pablo.pou@uam.es](mailto:pablo.pou@uam.es) (P. Pou).

bond and the other one remains unpaired. There is a semilocalized  $\pi$  state associated with the  $V_1$  which is close to the Fermi level that, in the case of an isolated  $V_1$ , could be either unoccupied, occupied by one electron –ferro or antiferromagnetically coupled with the  $\sigma$  electron– or double occupied. Therefore, the local magnetic moment, adding up the possible contributions from the  $\sigma$  and  $\pi$  states, could be  $0 \mu_B$  – $\sigma$  and  $\pi$  single occupied and antiferromagnetically coupled–,  $1 \mu_B$  –with an unoccupied or double occupied  $\pi$  state which would not contribute to the magnetic moment– or  $2 \mu_B$  – $\sigma$  and  $\pi$  single occupied and ferromagnetically coupled–.

However, simulations of point defects in extended systems computed imposing periodic boundary conditions (PBC), have a problem with the size of the cell [20]. In the case of graphene, small unit cells do not provide a proper description of the charge transfer from the  $\pi$  states of bulk graphene to the  $\pi$  states of the  $V_1$ . When using small cells, the limited number of bulk states that contribute to the charge transfer results in an artificial over-doping, reflected in the displacement of the Fermi level with respect to the extended states that shifts the Dirac point towards higher energies. Moreover, small cells allow the semilocalized  $\pi$  states of the vacancies to interact with each other. This spurious interaction contributes to the displacement and broadening of those defect states. Due to these effects, previous calculations have predicted the magnetic moment of a  $V_1$  to be  $<2 \mu_B$  [11,21–24]. Several works have reported results showing a reduction of the local magnetic moments upon cell size increasing [21,24]: they reach cell sizes up to 2.5 nm and it has been argued that the magnetism due to  $\pi$  orbitals should be quenched for low  $V_1$  concentrations [21]. On the other hand, calculations based on clusters show that the magnetic moment increases upon cluster size, pointing out to a  $2 \mu_B$  moment [24,25]. Therefore, calculations including periodicity seem to produce the opposite result of cluster based simulations.

We should also highlight that previous theoretical results have been calculated assuming ideal conditions with isolated and balanced graphene layers. However, the graphene layers are usually under strain due to the effect of the substrate or, in general, the environment. This effect could modify the properties induced by defects [26].

Regarding the mechanical properties of graphene, it has been reported that the Young's modulus of pristine graphene is around 1 TPa with an intrinsic breaking strength of 42 N/m [27] and it also presents a negative thermal expansion coefficient (TEC) [28,29]. Theoretical descriptions [4,30–32] predict a softness of the layer with the appearance of  $V_1$ . However, experiments based on atomic force microscopy (AFM) indentation have shown an increase of effective Young's modulus up to almost double the value for ideal graphene when the  $V_1$  content is  $\approx 0.2\%$  [12].

In this work we have performed a complete set of large scale DFT simulations, with cell sizes in the range of 1.5–7.4 nm, in order to shed some light on: i) the magnetism of an isolated  $V_1$ , ii) the influence of the strain on the magnetic properties of  $V_1$ , and iii) the effect of  $V_1$  on the mechanical properties of graphene. We have respectively found: i) a clear tendency of the local magnetization of a  $V_1$  towards a value of  $2 \mu_B$  for the diluted limit, ii) a structural and electronic transition of the  $V_1$  state when it is under an external in-plane tensile strain beyond the 2% and iii) a correlation between the strain field generated by the presence of the  $V_1$  and the partial suppression of out-of-plane fluctuations which leads to an increasing of the effective stiffness of the material for a low concentration of these defects.

With that purpose, we first present the methodology used on the simulations (see Section 2), of great importance given the crucial good scaling of the code used which enables us to work with large system sizes. We then tackle the problem of the magnetism of  $V_1$  on graphene (see Section 3). Next, we show the results of the

study of the  $V_1$  local magnetization dependency with an external in-plane strain (see Section 4). We finally show the strain field induced by the reconstruction of the  $V_1$ , which is consistent regardless of the cell size (see Section 5). We study how this can affect to the mechanical properties of the sheet analysing both the in-plane and out-of-plane deformations to correctly address the source of the stiffness increasing.

## 2. Methods

The calculations whose results are shown in this paper were done using the DFT OpenMX (Open source package for Material eXplorer) code [33,34]. The main advantage of this code, which uses pseudo-atomic localized basis functions, is that it has been carefully designed to be a powerful tool in large-scale ab initio electronic and structural calculations. Its parallelization scheme is based on a hybrid MPI/OpenMP approach which optimizes not only the CPU time consumption and scalability of the calculations but also the memory usage. Thus, systems with a few thousand atoms can be treated using the conventional diagonalization method. Our largest simulation performed in the Curie supercomputer was a  $G(30 \times 30)$  cell (1800 atoms) with a maximum k-point mesh of  $19 \times 19 \times 1$  for what 368 MPI and a threading of 8 were used (2944 processors in total).

We employed the generalized gradient approximation exchange-correlation density functional of Perdew, Burke, and Ernzerhof (PBE) [35] for the calculations. In order to be able to reach very large system sizes we restricted our basis to a  $DZ$  ( $s2p2$ ) after checking with some tests in the smaller systems that there were no big differences in the results performed with a  $DZP$  ( $s2p2d1$ ) basis or those computed with a plane waves code [36]. For both basis we used a cutoff radius of 6.0 a.u. The calculations were performed including spin polarization to be able to study the magnetization of the system, using an electronic temperature of 6 K. For the cell construction we used the lattice parameter obtained for the ideal graphene system of 248 pm.

For the first part of the study of the magnetization induced by the  $V_1$  for different cell sizes a real space grid equivalent to an energy cutoff of 200 Ry was used with a criteria for both electronic and ionic relaxations of  $1 \cdot 10^{-6}$  Hartree and  $1 \cdot 10^{-4}$  Hartree/bohr respectively. In order to study the evolution of the reconstruction of the  $V_1$  with the size of the cell, the structures of the  $G(6 \times 6)$ ,  $G(12 \times 12)$  and  $G(18 \times 18)$  were optimized using equivalent  $\Gamma$ -centered k-points meshes of  $13 \times 13 \times 1$ ,  $7 \times 7 \times 1$  and  $5 \times 5 \times 1$  respectively. In the latter we stopped the structural optimization at a slightly larger criterion ( $2 \cdot 10^{-4}$  Hartree/bohr) due to extremely long convergence times and for this reason no larger cells were structurally explored. For the study of the magnetization dependence with the cell and k-point mesh sizes, the  $G(6 \times 6)$  reconstruction was fixed for all of them and more atoms were added up to the specific cell size. The calculations performed were static.

For very large k-points meshes in the larger cells, some calculations (see Fig. 3) were stopped with an electronic convergence criterion of  $\approx 5 \cdot 10^{-5}$  Hartree always ensuring that the magnetization had converged up to  $1 \cdot 10^{-4} \mu_B$ .

Under typical experimental conditions, the interaction with the substrate where the graphene is grown or supported induces a finite strain. We have applied an external isotropic tensile strain to the system to analyse the possible influence of different experimental conditions in the properties of the graphene sheet. For the exhaustive study of the magnetization evolution with strain, a system consisting on two monovacancies ( $2V_1$ ) on a  $G(12 \times 12)$  cell was used. As the convergence of a single  $V_1$  per cell was very demanding, another  $V_1$  was added to the system and located in the other sublattice in such a way that the two vacancies were as far as

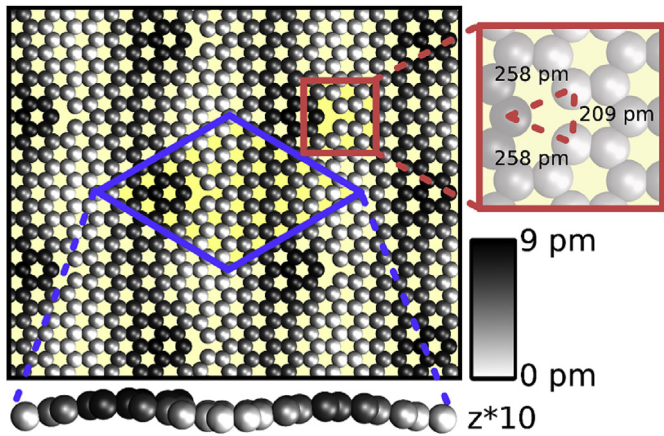


**Fig. 1.** Ball-and-stick scheme of the  $G(6 \times 6)$  cell structure (unit cell highlighted in blue) where the asymmetric reconstruction of the  $V_1$  can be seen ( $a-V_1$ ). The relevant distances between atoms of the  $V_1$  are shown in the zoom of the top view of the cell (red square). They can be compared to the reference ideal graphene distance which according to our calculations is 248 pm. In the side view the  $z$  coordinates have been multiplied by 10 to ease the visualization of the corrugation of the system which is around 9 pm. (A colour version of this figure can be viewed online.)

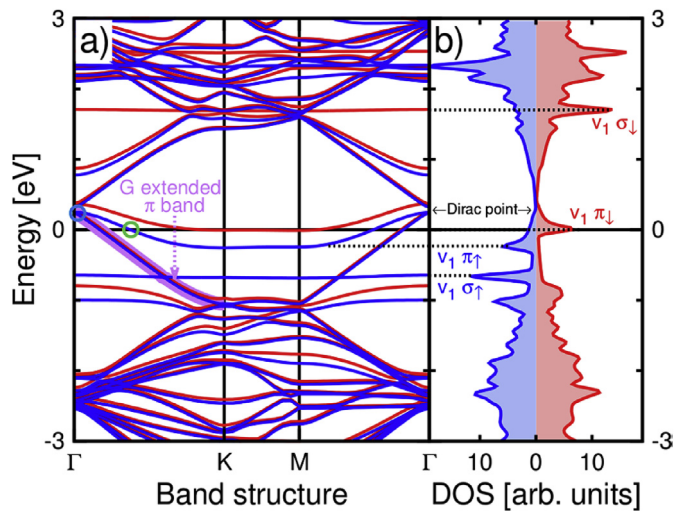


**Fig. 2.** a) Bands and b) DOS (calculated with a  $\Gamma$ -centered  $100 \times 100 \times 1$  k-point mesh) of the  $G(6 \times 6) + V_1$  cell as shown in Fig. 1. In a) the graphene extended  $\pi$  band is highlighted in purple. The blue circle shows the point where this band reaches the  $\Gamma$  point of the Brillouin zone, which denotes a shift of the Dirac point, and the green circle shows the Fermi wave vector ( $k_F$ ) of the  $V_1$  up- $\pi$  band. In both a) and b) the main states corresponding to the  $V_1$  are identified. (A colour version of this figure can be viewed online.)

possible to minimize interaction. This new system is easier to deal with in terms of structural and energy convergence. A  $5 \times 5 \times 1$  k-point mesh was used for the structure optimization while a larger  $11 \times 11 \times 1$  mesh was employed to get the electronic results; both calculations employed finer electronic and ionic relaxation criteria than in the previous part ( $1 \cdot 10^{-7}$  Hartree and  $5 \cdot 10^{-5}$  Hartree/bohr respectively). The study of the effect of the strain applied to the system requires changing the cell size. For this reason, we chose to fix the real space grid at (300, 300, 225) which corresponds to an energy cutoff of 350 Ry for a  $G(12 \times 12)$  with a strain of 5% ( $\approx 370$  Ry for the non-strained cell). In this study, we have considered the local magnetization of the vacancies as the average of the absolute values of magnetic moment for each of the two vacancies. This average cancels out the effect of a small asymmetry

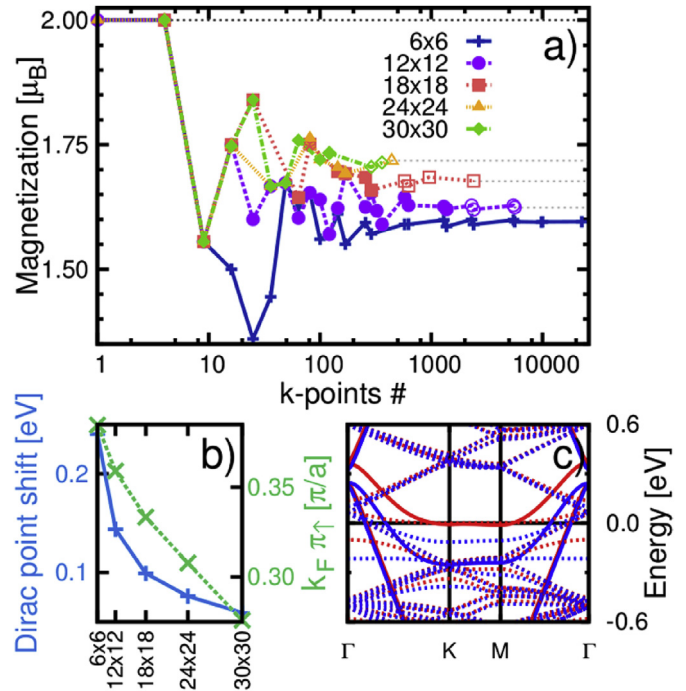


**Fig. 3.** a) Total magnetization for different cell sizes versus the number of k-points used to converge the calculations. The solid points have been calculated with an electronic convergence criterion of  $1 \cdot 10^{-6}$  Hartree while the open points have been calculated with  $5 \cdot 10^{-5}$  Hartree, however, the magnetization is always converged up to  $1 \cdot 10^{-4} \mu_B$ . b) Shift of the Dirac point (blue) and Fermi wave vector ( $k_F$ ) of the  $V_1$  up- $\pi$  band (green), both points highlighted in Fig. 2 for the  $G(6 \times 6) + V_1$  case. The best converged results for each of the cell sizes studied in a) are shown. c) Comparison of the bands – for the same energy range – of the smaller and bigger of all systems:  $G(6 \times 6) + V_1$  (solid lines) vs  $G(30 \times 30) + V_1$  (in dashed lines). (A colour version of this figure can be viewed online.)

in the filling of the four states (taking into account the  $k$ - $k$  symmetry) associated with the  $up-\pi_1$  (majority spin for vacancy 1) and  $down-\pi_2$  (majority spin for vacancy 2) bands close to the Fermi level. This asymmetry – that appears due to numerical errors that break the energy degeneracy of these two bands, and to the use of a  $k$ -sampling that includes the  $\Gamma$  point – induces a difference between the local magnetizations that scales as  $1/(\# \text{ of } k \text{ points})$ .

### 3. The magnetism of a single monovacancy on graphene

We start our study characterizing a small cell size,  $G(6 \times 6)$ , on which the vacancies are separated  $\approx 1.5$  nm, and their interaction is strong. We get the  $a-V_1$  reconstruction (see Fig. 1) where the soft bond distance is 209 pm and the formation energy 7.98 eV, in good agreement with previous results [4]. The graphene layer is not completely flat, it shows a topographic corrugation of 9 pm (see Fig. 1). With a k-point mesh of  $3 \times 3 \times 1$ , the  $V_1$  induces a magnetic moment of  $1.55 \mu_B$ , again in good agreement with previous results [11].

Its band structure and DOS are shown in Fig. 2. Both the localized  $\sigma$  bands, filled with one electron, and the semi-localized  $\pi$  states associated with the  $V_1$  are clearly identified. The  $\pi$  band, although very flat in some areas of the Brillouin zone, shows a broadening of  $\approx 75$  meV due to the interaction. The high  $V_1$  concentration has also modified the Dirac point (see the blue circle in Fig. 2a): i) it has been shifted towards positive energies ( $\approx 0.25$  eV) and ii) a small gap is opened between the two Dirac cones. Since the Dirac point is shifted towards positive energies, the extended states of graphene transfer charge to the  $\pi$  state of the  $V_1$ . However, due to

the broadening of this band, the  $up-\pi$  state is not able to accommodate all this transferred charge, so the rest of the electronic charge has to fill the next band which is the vacancy  $down-\pi$  state. As a consequence, the magnetic moment is less than  $2 \mu_B$  and the Fermi level is pinned in the  $down-\pi$  state. The precise value of the magnetic moment is, therefore, related with the Fermi wave vector ( $k_F$ )—the  $k$  vector of the last occupied state— associated with the extended band and the semi-localized  $V_1$   $up-\pi$  band. Both features depend on i) the  $k$ -mesh used in the calculation and ii) the size of the unit cell.

In Fig. 3a we show the values of the local magnetic moment as a function of the number of  $k$ -points used in the calculation for different cell sizes. We observed that the convergence with the  $k$ -point mesh is very slow, and it requires  $\approx 1000$   $k$ -points to reach converged values, much larger meshes than have previously been reported [4,11,21,25]. More importantly, as the  $\pi$  state associated with the  $V_1$  is semi-localized, its correct description requires a large number of  $k$ -points independently of the size of the cell. Our results show that, in the converged limit, the local magnetic moment increases with the cell size. Previous works have obtained the opposite result probably due to the  $k$ -mesh used in their calculations [21].

Fig. 3b shows the Dirac point shift as a function of the cell size. It tends to the Fermi level position for large sizes. The Fermi wave vector ( $k_F$ )—the  $k$  vector of the last occupied state— of the  $V_1$   $up-\pi$  band is also displaced towards the  $\Gamma$  point (see Fig. 3b), reducing the electron charge transferred from the  $up-\pi$  to the  $down-\pi$  band. Fig. 3c shows a comparison between the band structure of the  $G(6 \times 6) + V_1$  and  $G(30 \times 30) + V_1$  systems close to the Fermi level. The reduction of both the Dirac point shift and the broadening of  $V_1$   $\pi$  bands can be clearly observed. The exchange interaction between the  $\pi$  bands and the single-occupied  $\sigma$  state, i.e. the Hund's rule, breaks the spin symmetry and splits the two bands. Our results indicate that, in the limit of an isolated  $V_1$ , the splitting between the  $V_1$   $up-\pi$  and  $down-\pi$  bands is complete, leading to a completely filled  $V_1$   $up-\pi$  band and an empty  $V_1$   $down-\pi$  band, and, thus, a local magnetic moment of  $2 \mu_B$  ( $1 \mu_B$  from the flat sigma band plus  $1 \mu_B$  from this completely filled  $up-\pi$  band), as pointed out by the calculations carried out with large clusters [24,25]. This solves the discrepancy between the predictions based on DFT + PBC and DFT calculations using clusters [21,24,25].

We have to emphasize that our assignment of a local magnetic moment of  $2 \mu_B$  for the isolated vacancy limit requires the combination of two results: (i) the increasing values of the magnetization for larger unit cells shown in Fig. 3a, and (ii) the evolution with cell size of the Dirac point and the  $k_F$  of the  $V_1$   $up-\pi$  band illustrated in Fig. 3b and c, that points towards a complete filling in the limit of a single vacancy.

This very gradual evolution of the band is related with the slow spatial decay of the semilocalized state associated with the monovacancy. Even for our larger cell sizes, the semilocalized states from defects belonging to different cells are still interacting with each other. This effect is unavoidable in the type of calculation we are performing—DFT with periodic boundary conditions (PBC)— and produces a partial band filling. In the diluted limit— where these states do not interact with each other— they are either totally empty or totally filled, making the total magnetic moment to be either  $1 \mu_B$  or  $2 \mu_B$  respectively. In spite of their limitations, DFT-PBC calculations do allow us to determine the evolution of the filling of that band. Our results reveal a clear trend, slow but steady, in the magnetization and the evolution of the  $up-\pi$  band that suggests that this band is going to be completely filled in the limit of low defect concentration, leading to a magnetic moment of  $2 \mu_B$ .

These calculations for the evolution of the magnetic moment have been carried out by fixing the vacancy structure relaxed for

the  $G(6 \times 6)$  cell, but the possible influence of the changes in the relaxation for larger cells has also been considered. Our analysis shows that the main features of the structure, in particular the length of the soft bond, converge quite rapidly: this bond length is 209 pm in the  $G(6 \times 6)$ , decreases for the  $G(12 \times 12)$  down to 201 pm, and keeps a very similar value, 200 pm, for the  $G(18 \times 18)$ . Moreover, we have checked that the local magnetic moments obtained from fully relaxed calculations on these larger cells are almost identical to the ones determined from static calculations using the  $V_1$  structure relaxed for the smaller  $G(6 \times 6)$  unit cell. Thus, we have confirmed that, even for the cases where the soft bond distance is not totally converged, the local magnetic moment is not affected.

We have studied the stability of the  $a-V_1$  reconstruction versus the  $s-V_1$  structure of the  $V_1$  as experiments have reported both reconstructions [6,14,15,37]. The  $s-V_1$  reconstruction is not stable according to our calculations. Anyway, we have optimized the interatomic distances of the 3 atoms performing constrained calculations of this symmetric  $V_1$ . We found that the  $V_1$  is slightly expanded with respect to the ideal graphene lattice distances (250 pm vs 248 pm for the reference) and in this case there is no corrugation induced on the sheet. The energetic difference between this  $s-V_1$  configuration and the  $a-V_1$  stable reconstruction is around 350 meV for the  $G(6 \times 6)$  cell. Our DFT-MD simulations at room temperature show that the  $a-V_1$  reconstruction is maintained also at finite temperatures. These facts support the interpretation of the experimental evidence for a  $s-V_1$  reconstruction found with different experimental techniques (including STM [9] and TEM [15]) as a result of the overlap of the three possible  $a-V_1$  structure orientations of the  $V_1$ .

#### 4. Effects of isotropic in-plane strain in the magnetism of monovacancies

Real graphene sheets are not in their equilibrium state. The substrate, the boundary conditions, the temperature or the environment induce a strain field on the graphene layers. Moreover, strain engineering in graphene has been proposed to tune their electronic properties, in particular the magnetism [26,38]. Therefore, we have also studied the stability and the variation of the magnetic moments induced by the  $V_1$  as a function of an external isotropic strain applied to the layer. We have fixed our attention in the stretching as previous works focused on other regimes [26].

The large computational cost required to converge the previous calculations prohibited this characterization in the systems (a single  $V_1$  per unit cell) showed above. We have realized that the electronic convergence is faster for  $V_1$  coupled antiferromagnetically, this occurs when the  $V_1$  are located in different graphene sublattices. Also, the size of the unit cell cannot be very large. Therefore, due to these limitations, we have carried out the study of strain in a  $G(12 \times 12)$  cell with two  $V_1$  in opposite sublattices (see Fig. 4).

We have applied an in-plane strain, relaxing all the atoms and calculating the local magnetic moment associated with each  $V_1$ . As the vacancies interact with each other, we have obtained their local magnetic moment as the addition of the moments of the atoms inside a region around each  $V_1$ . These regions, highlighted in yellow and magenta in the ball-and-stick model inside the bottom panel of Fig. 4, have been chosen to treat both vacancies on an equal footing and maximize the number of atoms that contribute to the calculation, avoiding any overlap between the areas associated to each defect.

In Fig. 4 we also show the absolute value of the average local magnetic moment of a  $V_1$  as a function of the applied strains. The higher panels show the spin density map around the vacancies, as

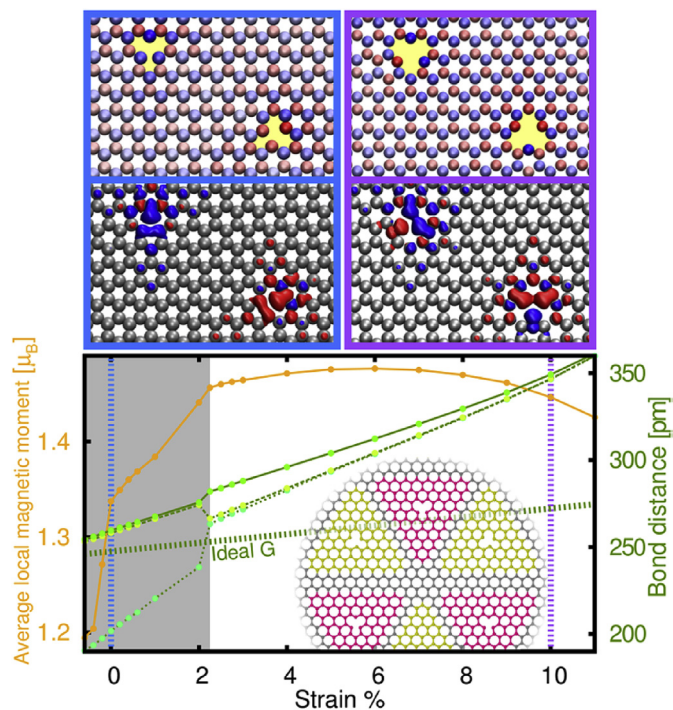


**Fig. 4.** (bottom) Local magnetization (orange) and evolution of the distances between the three atoms of the  $V_1$  (green) for the  $G(12 \times 12) + 2V_1$  system. We have included a reference dashed line (also in green) with distances corresponding to a pristine graphene layer under strain. The atoms of the equivalent regions used to calculate the local magnetization of each  $V_1$  are shown in the ball-and-stick scheme inside the plot (highlighted in yellow and magenta). In the gray area, the  $a-V_1$  (asymmetric) structure found at the equilibrium is preserved while for the rest of the plot the most favourable solution is the  $qs-V_1$ . Atomic magnetic moments (upper panel) and spin density (lower panel) for the  $a-V_1$  structure at 0% strain (framed in blue) and the  $qs-V_1$  configuration at 10% strain (framed in purple) are shown. In the upper panels, each atom is painted in blue or red depending on its total magnetic polarization according to the Mulliken spin populations. The darker the colour of the atom (either blue or red) the higher the magnetic moment for this atom. The location of the  $V_1$  is highlighted in yellow. Below each magnetization map we show the spin density of the same region. Maps for strain values corresponding to the same  $V_1$  structure are alike. (A colour version of this figure can be viewed online.)

well as the moments associated with the atoms. The gray area in Fig. 4 emphasizes the region (strains <2%) where the same 5–9  $a-V_1$  solution [11] found in the equilibrium state (strain of 0%) is preserved. The  $V_1$  of this system at a strain of 0% present a soft-bond distance of 201 pm and as higher strains are applied the soft dimer bond is elongated but still exists (see green lines in Fig. 4). In this region the local magnetic moment of the  $V_1$  increases  $\approx 9\%$  with respect to the equilibrium upon extension ( $\approx 2\%$ ) and abruptly decreases upon compression in agreement with previous results [26].

Around a stretching strain of 2% we can see a transition into a different solution. This new state is mainly characterized by a change in the reconstruction of the vacancies which turns into a structure close to the  $s-V_1$  configuration, where the soft bond has effectively disappeared, and the distances among the three atoms in the  $V_1$  are very similar (e.g. 294 pm, 294 pm and 304 pm for a 5% strain). Thus, we will denominate it as quasi-symmetric reconstruction ( $qs-V_1$ ). The higher the strain the closer the reconstruction is to a  $s-V_1$ . Fig. 4 shows the structural evolution of the  $V_1$  through the bond distances between the three atoms surrounding it which can be compared. The plot also shows a comparison against the corresponding values for pristine graphene.

While the new  $qs-V_1$  structure is geometrically more

symmetric, the opposite happens with the magnetic distribution. The local spin density shows two atoms of the  $V_1$  occupied by the majority spin and the other by the minority spin. In spite of this change in the magnetic distribution, the total magnetic moment remains fairly constant, reaching a saturation value  $\approx 10\%$  larger than the value in the equilibrium. This high-strain solution is stable up to strains of 12% where the structure of the full sheet is broken with the cracks starting in the vacancy.

The transition between solutions takes place due to the competition between the magnetic and mechanical contributions to the energy depending on the strain. Beyond the 2% strain the Jahn-Teller distortion that created the 5–9 reconstruction becomes unstable since the double occupied  $\sigma$  state associated with the soft dimer bond increases its energy upon stretching. Then, a new magnetic solution [26] –associated with a new way to fill the states created by the  $V_1$ – becomes comparable in energy with the previous solution. This new configuration is characterized by the filling of the three  $\sigma$  states associated with each atom of the  $V_1$  with just one electron –2 of them with majority spin and the other with the minority one– leaving the total magnetism associated with the  $\sigma$  states equal to  $1 \mu_B$  as in the previous solution. On the other hand, the semi-localized  $\pi$  state is mainly occupied with the majority spin. As a result, the spin behaviour is as showed in the spin maps in Fig. 4. For strains larger than 3%, this new solution becomes the most stable as can be seen in Fig. 5 where energy differences between solutions are shown.

We have seen how the magnetization of graphene with  $V_1$  defects changes by applying an external in-plane strain to the system. The magnetism is stable and does not disappear with the strain. We mainly see a decrease upon compression and an increase upon extension of the layer. Apart from the known  $a-V_1$  solution for lower strains, we have found a transition to a  $qs-V_1$  structure around strains of 2% that is characterised by a new magnetic distribution with the three  $\sigma$  states associated with the  $V_1$  single electronically occupied. Moreover, we have explored a different arrangement of  $V_1$  to analyse the influence of the relative location on these defects obtaining very similar results.

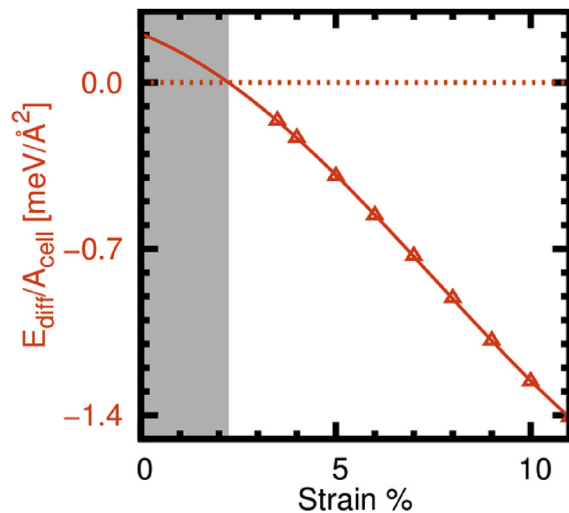


**Fig. 5.** Energy difference for the two different spin distributions studied for the  $G(12 \times 12) + 2V_1$  system: the  $a-V_1$  and the  $qs-V_1$ . The points represented have been computed for cases on which we have managed to converge both solutions. The solid line has been calculated through the subtraction of the fitting curves of the energy data for each solution. This curve not only reproduces remarkably well the calculated points but predicts quite accurately the transition state and the behaviour in the low-strain side. According to this curve the  $a-V_1$  solution is stable up to a  $\approx 2\%$  strain (range highlighted with a grey shadow). (A colour version of this figure can be viewed online.)

## 5. Mechanical properties of graphene tailored with monovacancies

Monovacancies, besides inducing magnetism in graphene, can also tune its mechanical properties even at low concentrations [12]. AFM microscopy indentation experiments have concluded that a low concentration of  $V_1$  in graphene increases its effective stiffness and reduces its fracture strength [12].

The latter is an expected behaviour for defected covalent solids and it can be explained by classical mechanics [4,31]. However, the modifications observed in the effective Young's modulus are unexpected and its origin is still unclear. It has been suggested that this behaviour is due to the dependency of the mechanical properties of 2D membranes on the flexural modes and thermal fluctuations. However, a fundamental, atomistic explanation is still missing. Our large scale simulations of  $V_1$  in graphene allow us to compute the real 2D Young modulus, the strain fields generated by the  $V_1$  and their effect in the out-of-plane modes. The analysis of these results sheds light on the origin of the experimental observations.

### 5.1. Effect of the monovacancies in the graphene mechanical in-plane response

The calculated energy variations per unit cell of both the pristine layer and the  $G(12 \times 12) + 2V_1$  system as a function of an isotropic in-plane strain applied to the layer are shown in Fig. 6. The defect has slightly shifted the minimum towards negative strains. The inset of Fig. 6 shows the energy variation when stretching the layer up to the rupture. The failure strain is  $\approx 12\%$ , smaller than in pristine graphene ( $>20\%$ ) and in agreement with previous results [39–41]. The green curve is the derivative of the energy variation with respect to the strain. Total-energy calculations of graphene give access to the 2D bulk modulus,  $B$ , through the relation

$$\frac{\Delta E}{A_{\text{cell}}} = \frac{B}{2} \left( \frac{\Delta A_{\text{cell}}}{A_{\text{cell}}} \right)^2. \quad (1)$$

$\Delta E$  corresponds to the energy differences and  $\Delta A_{\text{cell}}$  to the change of the unit-cell area  $A_{\text{cell}}$  obtained by an assumed tension.

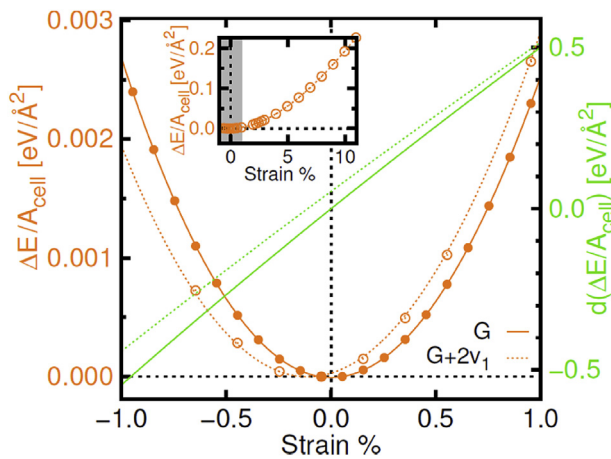


**Fig. 6.** Comparison between the energy response to an isotropic in-plane strain of the  $G(12 \times 12)$  and the  $G(12 \times 12) + 2V_1$  systems. The energy variation curve is shown in orange and the derivative of this energy with respect to the strain is depicted in green (solid/open circles are the calculated data for  $G(12 \times 12)/G(12 \times 12) + 2V_1$ , solid/dashed lines are the respective 4th order polynomial fits). In the inset, we show the energy variation curve for the full range on which calculations for the  $G(12 \times 12) + 2V_1$  were performed. A grey shade marks the strain region shown in the main plot. (A colour version of this figure can be viewed online.)

The 2D bulk modulus can be written in terms of the Young's modulus for 2D samples,  $E_{2D}$ , and the in-plane Poisson coefficient,  $\nu$  (taken here as 0.165, the Poisson's ratio for graphite in the basal plane [42]), as follows

$$B = \frac{E_{2D}}{2(1 - \nu)}. \quad (2)$$

In turn,  $E_{2D}$ , can be expressed in terms of the elastic constants  $C_{11}$ ,  $C_{12}$  and an arbitrary thickness of the graphene monolayer  $h$  (usually taken as the graphite interlayer distance,  $h = 335$  pm) as

$$E_{2D} = h \frac{C_{11}^2 - C_{12}^2}{C_{11}}. \quad (3)$$

As expected, but contrary to the experimental results, the pristine graphene ( $E_{2D} = 349$  N/m,  $B = 209$  N/m) is stiffer than the defective graphene ( $E_{2D} = 321$  N/m,  $B = 192$  N/m).

The results that we present are simulations that can be compared with an ideal system at zero or very low temperature. However, experiments are done at room temperature and, in membranes and 2D materials, thermal fluctuations play a relevant role in the mechanical properties [43–45]. The energy dispersion of the flexural modes induces important out-of-plane corrugations with large wave lengths in the layers. Moreover, the out-of-plane modes depend on the in-plane strain field [45–47]. So the question that arises is: could the  $V_1$  induce a strain field able to modify the out-of-plane modes and, therefore, the mechanical properties of graphene layers at finite temperatures?

### 5.2. The strain field induced by monovacancies in graphene

We have calculated, as a representation of the strain field, the average bond distance map for different  $V_1$  concentrations and external strains. We have defined the average bond distance as the mean nearest-neighbour distance of each atom referred to the ideal graphene nearest-neighbour distance for each of the external strains applied. In Fig. 7a, we show the result for the  $G(6 \times 6) + V_1$  system. Blue atoms have larger average bond distances than in pristine graphene whereas red atoms have shorter average bond distances. The Jahn-Teller distortion induces the formation of the soft bond and, as a consequence, the graphene lattice at both sides of the bond is stretched. On the contrary, in the perpendicular direction of the soft bond the atoms around the  $V_1$  (in red) are compressed in a figure-of-8-like structure.

Upon reduction of  $V_1$  concentration (simulated by increasing the unit cell size), a similar strain field appears. However, while the compressed 8-shaped area remains localized around the  $V_1$  and does not significantly depend on  $V_1$  concentration, the stretched area spreads in a larger region around the  $V_1$  as the cell size is increased (see Fig. 7a–e for the  $G(6 \times 6) + V_1$ , the two  $G(12 \times 12) + 2V_1$  with  $V_1$  in different arrangements, the  $G(12 \times 12) + V_1$  and the  $G(18 \times 18) + V_1$  cells). Most importantly, in all cases, the stretching of the lattice is always predominant over the compression. This total effect is also confirmed by the displacement of the energy minimum, with respect to the clean graphene case, towards negative strain values as shown in Fig. 6.

We have also studied the effect of the  $V_1$  arrangement in the induced strain fields. In the  $G(12 \times 12) + 2V_1$  system we have tested two different arrangements (see Fig. 7b,c). The main results explained above related with the stretched/compressed areas still hold for both distributions. However, the results point out that the induced strain fields are controlling the atomic structure of the ground state: after careful optimization of the structures, the soft bond is formed between the two atoms of each  $V_1$  such that the overlap of both compressed areas and each stretched area with the

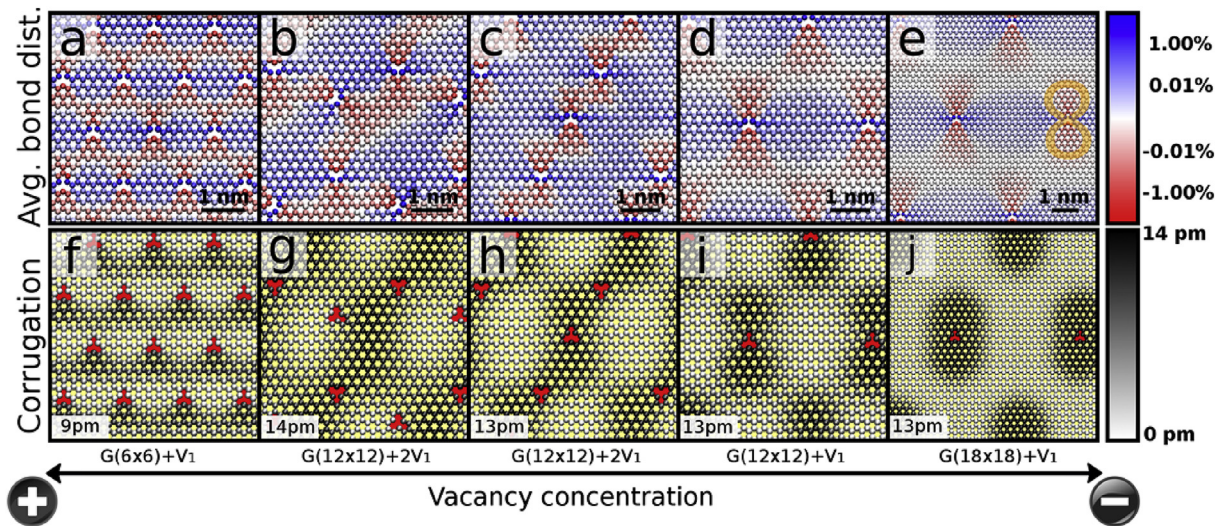


**Fig. 7.** Comparison between the average bond distance map (top panels) and corrugation (bottom panels) for different  $V_1$  concentrations ( $G(6 \times 6) + V_1$ ,  $G(12 \times 12) + 2V_1$ ,  $G(12 \times 12) + V_1$  and  $G(18 \times 18) + V_1$ ) and different vacancies arrangements (two different ones for the  $G(12 \times 12) + 2V_1$  case). In the average bond distance maps, the red colour corresponds to compressed atoms (closer to their nearest neighbours than in pristine graphene) and the stretched atoms (farther than in the perfect surface) are depicted in blue, being most of the atoms around a  $\pm 0.5\%$ . The 8 shape of the compressed region is highlighted in orange for the lowest concentration case. In the corrugation maps the locations of the  $V_1$  are highlighted in red and the corrugation value (represented by the difference between the black and white atoms in the colour scale) for each case is provided. (A colour version of this figure can be viewed online.)

compressed area of the other  $V_1$  are minimized. Therefore, the  $V_1$  are interacting through their induced strain fields.

In Fig. 7f–j we also show the corrugation map for each case. The creation of the reconstructed vacancy induces a stress in the graphene layer. This stress is relaxed by inducing both an in-plane strain field and a small out-of-plane deformation of the layer. This corrugation pattern does not follow the in-plane strain field but is mostly controlled by the boundary conditions, i.e. the cell shape. This is clearly seen comparing the two  $G(12 \times 12) + 2V_1$  cases (Fig. 7b,c,g and h): the corrugation maps are very similar whereas the strain field is significantly affected by the  $V_1$  location and orientation. The induced corrugation converges to  $\approx 13$  pm for unit cells larger than the  $G(12 \times 12)$  case.

Furthermore, we have also checked that an applied external strain does not substantially modify the average bond distance maps in the range where the 5–9 reconstruction is preserved. In our calculations on the  $G(12 \times 12) + 2V_1$  system, the bond stands the extra stretching of the lattice up to an external strain of 2%.

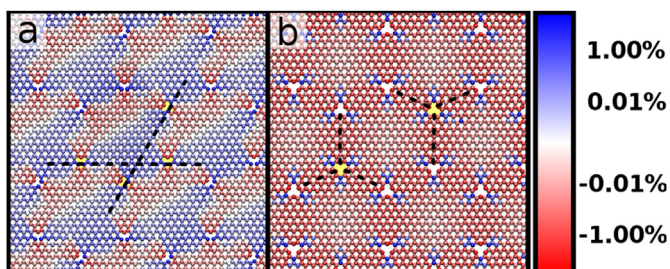


**Fig. 8.** a) Average bond distance map for the  $G(12 \times 12) + 2V_1$  system at the equilibrium (0% strain). b) Average bond distance map for the same system at a strain of 10%. In the average bond distance maps, bonds shorter than the distance of the strained ideal graphene are coloured in red while the stretched bonds are painted in blue. In the case of the equilibrium solution the dimer is regarded as a bonded pair of atoms, that is the reason why is depicted in blue (stretched). In both maps the symmetry of the correspondent deformation field is depicted with black dashed lines. In all cases the position of an example  $V_1$  of each sublattice is highlighted in yellow. (A colour version of this figure can be viewed online.)

Then, it breaks and the reconstruction changes to the  $qs-V_1$  structure inducing changes in the strain field generated by the  $V_1$ : the bonds (compared to the strained pristine graphene bonds) are now compressed (see Fig. 8). However, for most cases, in particular for thermal fluctuations and AFM indentation experiments [12,27,46] strains suffered by a graphene layer in a realistic environment are much smaller than 2%.

In conclusion, our results show that the  $V_1$  are effectively stretching the layer. Next, we show how this  $V_1$ -induced strain field

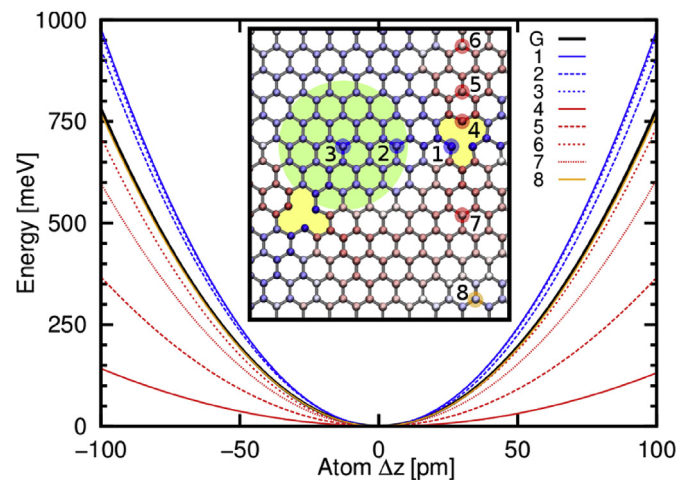


**Fig. 9.** Out-of-plane energy curves for atoms in different regions of the  $V_1$ -induced strain field. The ball-and-stick scheme shows the location of the atoms analysed which are depicted in the same colour as its corresponding energy curve. In the calculations we fix the given atom at a certain  $\delta z$  displacement with respect to its equilibrium height and optimize the structure within a radius of 573 pm. The rest of the atoms of the sheet are also fixed during the optimization. As an example, a circle containing all the atoms that have been relaxed in the calculations around the atom 3 has been highlighted in green. The location of the  $V_1$  is painted in yellow. The colour code (red for compressed bond atoms and blue for stretched bond atoms) used for the average bond distance maps is preserved to ease visualization and comparison. (A colour version of this figure can be viewed online.)

modifies the strength of the out-of-plane modes.

### 5.3. Monovacancy-induced strain field effect on out-of-plane deformations

The effect of the  $V_1$  in the out-of-plane modes can be seen in Fig. 9. The energy curves for small out-of-plane displacements are calculated for atoms located in the compressed, stretched and neutral areas of the  $G(12 \times 12) + 2V_1$  strain field map (the strain field colour code is included in the ball-and-stick scheme of Fig. 9). The pristine graphene energy curve is shown also as a reference (black curve in Fig. 9). For an atom in the neutral area we exactly recover what we had for the ideal system (see orange line in Fig. 9). For atoms in the stretched areas (which take up most of the sheet surface), we clearly see an increasing of the stiffness while the compressed areas present a softer behaviour. Therefore, our calculations point out that the extra strain induced by the presence of the  $V_1$  in the sheet makes the system stiffer for out-of-plane displacements than the ideal system. As a consequence, this could quench some of the fluctuations of the graphene layer and tune the mechanical properties related with the thermal fluctuations as the effective stiffness [12] or the negative thermal expansion coefficient [45,48].

## 6. Conclusions

We have analysed the magnetic and mechanical properties induced by  $V_1$  in graphene. We have concluded that the magnetization of the system for low  $V_1$  concentrations tends to a value of  $2 \mu_B$ , contrary to previous works in extended systems calculated with PBC, and supporting the results of cluster calculations. This discrepancy can be explained in terms of the huge cell size and fine k-point meshes required to converge the magnetism of the system in calculations with extended systems. Moreover, we have seen that the magnetism of a  $V_1$  can be tuned by applying an external in-plane strain getting an increasing of a 10% on the magnetization upon stretching. We have found a transition around a strain of 2% between the well-known  $a-V_1$  solution and a  $qs-V_1$ , one on which the soft dimer bond of the  $a-V_1$  reconstruction is broken, leading to an almost symmetric configuration with a different electronic structure.

We have also shown that the  $V_1$  affect the mechanical properties through the strain field induced by the soft bond that stretches the graphene lattice around the  $V_1$ . Our results show that this stretching stiffens the out-of-plane modes of the layer. This extra energy cost quenches these fluctuations, possibly leading to an increase of the effective stiffness of the graphene and to the reduction of the absolute value of the negative thermal expansion coefficient in defective graphene samples.

## Acknowledgements

We thank G. Vilhena, J. Gómez-Herrero and C. Gómez-Navarro for fruitful discussion. We acknowledge financial support from the Spanish MINECO (Grants CSD2010-00024, MAT2011-23627 and MAT2014-54484-P). P. P. was supported by the Ramón y Cajal program. Computer time provided by the PRACE research infrastructure in the Curie supercomputer and also by the Spanish Supercomputing Network (RES) in the MareNostrum III supercomputer (BSC, Barcelona) is gratefully acknowledged.

## References

- [1] A.H. Castro Neto, F. Guinea, N.M.R. Peres, K.S. Novoselov, A.K. Geim, The electronic properties of graphene, *Rev. Mod. Phys.* 81 (2009), <http://dx.doi.org/10.1103/RevModPhys.81.109>.
- [2] W. Han, R.K. Kawakami, M. Gmitra, J. Fabian, Graphene spintronics, *Nat. Nanotechnol.* 9 (2014), <http://dx.doi.org/10.1038/nnano.2014.214>.
- [3] L. Liu, M. Qing, Y. Wang, S. Chen, Defects in graphene: generation, healing, and their effects on the properties of graphene: a review, *J. Mater. Sci. Technol.* 31 (6) (2015) 599–606, <http://dx.doi.org/10.1016/j.jmst.2014.11.019>.
- [4] S.T. Skowron, I.V. Lebedeva, A.M. Popov, E. Bichoutskaia, Energetics of atomic scale structure changes in graphene, *Chem. Soc. Rev.* 44 (2015) 3143, <http://dx.doi.org/10.1039/C4CS00499J>.
- [5] J. Lahiri, Y. Lin, P. Bozkurt, I.I. Oleynik, M. Batzill, An extended defect in graphene as a metallic wire, *Nat. Nanotechnol.* 5 (2010) 326, <http://dx.doi.org/10.1038/nnano.2010.53>.
- [6] A. Hashimoto, K. Suenaga, A. Gloter, K. Urita, S. Iijima, Direct evidence for atomic defects in graphene layers, *Nature* 430 (2004) 870, <http://dx.doi.org/10.1038/nature02817>.
- [7] H. Terrones, R. Lv, M. Terrones, M.S. Dresselhaus, The role of defects and doping in 2D graphene sheets and 1D nanoribbons, *Rep. Prog. Phys.* 75 (2012) 062501, <http://dx.doi.org/10.1088/0034-4885/75/6/062501>.
- [8] F. Banhart, J. Kotakoski, A.V. Krashennnikov, Structural defects in graphene, *ACS Nano* 5 (2010), <http://dx.doi.org/10.1021/nn102598m>.
- [9] A.A. El-Barbary, R.H. Telling, C.P. Ewels, M.I. Heggie, P.R. Briddon, Structure and energetics of the vacancy in graphite, *Phys. Rev. B* 68 (2003) 144107, <http://dx.doi.org/10.1103/PhysRevB.68.144107>.
- [10] Y. Ma, P.O. Lehtinen, A.S. Foster, R.M. Nieminen, Magnetic properties of vacancies in graphene and single-walled carbon nanotubes, *New J. Phys.* 6 (2004) 68, <http://dx.doi.org/10.1088/1367-2630/6/1/068>.
- [11] O.V. Yazyev, L. Helm, Defect-induced magnetism in graphene, *Phys. Rev. B* 75 (12) (2007), <http://dx.doi.org/10.1103/PhysRevB.75.125408>.
- [12] G. López-Polín, C. Gómez-Navarro, V. Parente, F. Guinea, M.I. Katsnelson, F. Pérez-Murano, J. Gómez-Herrero, Increasing the elastic modulus of graphene by controlled defect creation, *Nat. Phys.* 11 (1) (2015) 2631, <http://dx.doi.org/10.1038/NPHYS3183>.
- [13] M. Neek-Amal, F.M. Peeters, Linear reduction of stiffness and vibration frequencies in defected circular monolayer graphene, *Phys. Rev. B* 81 (2010) 235437, <http://dx.doi.org/10.1103/PhysRevB.81.235437>.
- [14] J.C. Meyer, C. Kisielowski, R. Erni, M.D. Rossell, M.F. Crommie, A. Zettl, Direct imaging of lattice atoms and topological defects in graphene membranes, *Nano Lett.* 8 (2008) 3582–3586, <http://dx.doi.org/10.1021/nl801386m>.
- [15] A.W. Robertson, B. Montanari, K. He, C.S. Allen, Y.A. Wu, N.M. Harrison, A.I. Kirkland, J.H. Warner, Structural reconstruction of the graphene monovacancy, *ACS Nano* 7 (2013) 4495–4502, <http://dx.doi.org/10.1021/nn401113r>.
- [16] A.W. Robertson, J.H. Warner, Atomic resolution imaging of graphene by transmission electron microscopy, *Nanoscale* 5 (2013) 4079–4093, <http://dx.doi.org/10.1039/c3nr00934c>.
- [17] M.M. Ugeda, I. Brihuega, F. Guinea, J.M. Gómez-Rodríguez, Missing atom as a source of carbon magnetism, *Phys. Rev. Lett.* 104 (2010) 096804, <http://dx.doi.org/10.1103/PhysRevLett.104.096804>.
- [18] M.M. Ugeda, D. Fernández-Torre, I. Brihuega, P. Pou, A.J. Martínez-Galera, R. Pérez, J.M. Gómez-Rodríguez, Point defects on graphene on metals, *Phys. Rev. Lett.* 107 (11) (2011), <http://dx.doi.org/10.1103/PhysRevLett.107.116803>.
- [19] T. Kondo, Y. Honma, J. Oh, T. Machida, J. Nakamura, Edge states propagating from a defect of graphite: scanning tunneling spectroscopy measurements, *Phys. Rev. B* 82 (2010) 153414, <http://dx.doi.org/10.1103/PhysRevB.82.153414>.
- [20] C. Freysoldt, B. Grabowski, T. Hickel, J. Neugebauer, G. Kresse, A. Janotti, C.G. Van de Walle, First-principles calculations for point defects in solids, *Rev. Mod. Phys.* 86 (2014), <http://dx.doi.org/10.1103/RevModPhys.86.253>.
- [21] J.J. Palacios, F. Ynduráin, Critical analysis of vacancy-induced magnetism in monolayer and bilayer graphene, *Phys. Rev. B* 85 (2012) 245443, <http://dx.doi.org/10.1103/PhysRevB.85.245443>.
- [22] C.-C. Lee, Y. Yamada-Takamura, T. Ozaki, Competing magnetism in Pi-electrons in graphene with a single carbon vacancy, *Phys. Rev. B* 90 (1) (2014), <http://dx.doi.org/10.1103/PhysRevB.90.014401>.
- [23] J.-J. Chen, H.-C. Wu, D.-P. Yu, Z.-M. Liao, Magnetic moments in graphene with vacancies, *Nanoscale* 6 (2014) 8814, <http://dx.doi.org/10.1039/c3nr06892g>.
- [24] M. Casartelli, S. Casolo, G.F. Tantarini, R. Martinazzo, Spin coupling around a carbon atom vacancy in graphene, *Phys. Rev. B* 88 (2013) 195424, <http://dx.doi.org/10.1103/PhysRevB.88.195424>.
- [25] B. Wang, S.T. Pantelides, Magnetic moment of a single vacancy in graphene and semiconducting nanoribbons, *Phys. Rev. B* 86 (2012) 165438, <http://dx.doi.org/10.1103/PhysRevB.86.165438>.
- [26] E.J.G. Santos, S. Riikonen, D. Sánchez-Portal, A. Ayuela, Magnetism of single vacancies in rippled graphene, *J. Phys. Chem. C* 116 (2012) 7602–7606, <http://dx.doi.org/10.1021/jp300861m>.
- [27] C. Lee, X. Wei, J.W. Kysar, J. Hone, Measurement of the elastic properties and intrinsic strength of monolayer graphene, *Science* 321 (2008) 5887, <http://dx.doi.org/10.1126/science.1157996>.
- [28] N. Mounet, N. Marzari, First-principles determination of the structural, vibrational and thermodynamic properties of diamond, graphite, and derivatives, *Phys. Rev. B* 71 (2005) 205214, <http://dx.doi.org/10.1103/PhysRevB.71.205214>.
- [29] D. Yoon, Y.-W. Son, H. Cheong, Negative thermal expansion coefficient of graphene measured by Raman spectroscopy, *Nano Lett.* 11 (2011) 3227,

- <http://dx.doi.org/10.1021/nl201488g>.
- [30] A.S. Fedorov, Z.I. Popov, D.A. Fedorov, N.S. Eliseeva, M.V. Serjantova, A.A. Kuzubov, DFT investigation of the influence of ordered vacancies on elastic and magnetic properties of graphene and graphene-like SiC and BN structures, *Phys. Status Solidi B* 249 (2012) 2549.
- [31] S.K. Georgantzinos, D.E. Katsareas, N.K. Anifantis, Limit load analysis of graphene with pinhole defects: a nonlinear structural mechanics approach, *Int. J. Mech. Sci.* 55 (2012) 85, <http://dx.doi.org/10.1016/j.ijmecsci.2011.12.006>.
- [32] N. Jing, Q. Xue, C. Ling, M. Shan, T. Zhang, X. Zhou, Z. Jiaob, Effect of defects on Young's modulus of graphene sheets: a molecular dynamics simulation, *Rsc. Adv.* 2 (2012) 9124, <http://dx.doi.org/10.1039/C2RA21228E>.
- [33] T. Ozaki, Variationally optimized atomic orbitals for large-scale electronic structures, *Phys. Rev. B* 67 (2003) 155108, <http://dx.doi.org/10.1103/PhysRevB.67.155108>.
- [34] T. Ozaki, H. Kino, Numerical atomic basis orbitals from H to Kr, *Phys. Rev. B* 69 (2004) 195113, <http://dx.doi.org/10.1103/PhysRevB.69.195113>.
- [35] J.P. Perdew, K. Burke, M. Ernzerhof, Generalized gradient approximation made simple, *Phys. Rev. Lett.* 77 (1996) 3865, <http://dx.doi.org/10.1103/PhysRevLett.77.3865>.
- [36] G. Kresse, J. Furthmüller, Efficient iterative schemes for Ab initio total-energy calculations using a plane-wave basis set, *Phys. Rev. B* 54 (1996) 11169, <http://dx.doi.org/10.1103/PhysRevB.54.11169>.
- [37] O. Lehtinen, I.-L. Tsai, R. Jalil, R.R. Nair, J. Keinonen, U. Kaiser, I.V. Grigorieva, Non-invasive transmission electron microscopy of vacancy defects in graphene produced by ion irradiation, *Nanoscale* 6 (2014) 6569, <http://dx.doi.org/10.1103/PhysRevB.90.014401>.
- [38] N. Levy, S.A. Burke, K.L. Meaker, M. Panlasigui, A. Zettl, F. Guinea, A.H.C. Neto, M.F. Crommie, Strain-induced pseudo-magnetic fields greater than 300 Tesla in graphene nanobubbles, *Science* 329 (2010) 544–547, <http://dx.doi.org/10.1126/science.1191700>.
- [39] P. Zhang, L. Ma, F. Fan, Z. Zeng, C. Peng, P.E. Loya, Z. Liu, Y. Gong, J. Zhang, X. Zhang, P.M. Ajayan, T. Zhu, J. Lou, Fracture toughness of graphene, *Nat. Commun.* 5 (2014), <http://dx.doi.org/10.1038/ncomms4782>.
- [40] F. Liu, P.M. Ming, J. Li, Ab initio calculation of ideal strength and phonon instability of graphene under tension, *Phys. Rev. B* 76 (2007) 064120, <http://dx.doi.org/10.1103/PhysRevB.76.064120>.
- [41] R. Khare, S.L. Mielke, J.T. Paci, S. Zhang, R. Ballarini, G.C. Schatz, T. Belytschko, Coupled quantum mechanical/molecular mechanical modeling of the fracture of defective carbon nanotubes and graphene sheets, *Phys. Rev. B* 75 (2007) 075412, <http://dx.doi.org/10.1103/PhysRevB.75.075412>.
- [42] O.L. Blakslee, D.G. Proctor, E.J. Seldin, G.B. Spence, T. Weng, Elastic constants of compression-annealed pyrolytic graphite, *J. Appl. Phys.* 41 (8) (1970) 3373–3382, <http://dx.doi.org/10.1063/1.1659428>.
- [43] J.A. Aronovitz, T.C. Lubensky, Fluctuations of solid membranes, *Phys. Rev. Lett.* 60 (1988) 2634, <http://dx.doi.org/10.1103/PhysRevLett.60.2634>.
- [44] D. Nelson, T. Piran, S. Weinberg, *Statistical Mechanics of Membranes and Surfaces*, World Scientific, Singapore, 2004, <http://dx.doi.org/10.1002/acp.1990.010410813>.
- [45] M.I. Katsnelson, A. Fasolino, Graphene as a prototype crystalline membrane, *Acc. Chem. Res.* 46 (2013) 97, <http://dx.doi.org/10.1021/ar300117m>.
- [46] G. López-Polín, M. Jaafar, F. Guinea, R. Roldán, C. Gómez-Navarro, G.-H. J., Strain Dependent elastic modulus of graphene, arXiv:1504.05521.
- [47] R. Roldán, A. Fasolino, K.V. Zakharchenko, M.I. Katsnelson, Suppression of anharmonicities in crystalline membranes by external strain, *Phys. Rev. B* 83 (2011) 174104, <http://dx.doi.org/10.1103/PhysRevB.83.174104>.
- [48] K.V. Zakharchenko, M.I. Katsnelson, A. Fasolino, Finite temperature lattice properties of graphene beyond the quasiharmonic approximation, *Phys. Rev. Lett.* 102 (2011) 046808, <http://dx.doi.org/10.1103/PhysRevLett.102.046808>.